Hierarchical behavior control by a single class of interneurons

Jing Huo[1,2,3,*], **Tianqi Xu**[1,2,*,✉], **Mahiber Polat**[1,2,*], **Xiaoqian Zhang**[1,2], **and Quan Wen**[1,2,✉]

[1]Division of Life Sciences and Medicine, University of Science and Technology of China, Hefei, China

[2]Hefei National Laboratory for Physical Sciences at the Microscale, Center for Integrative Imaging, University of Science and Technology of China, Hefei, China

[3]School of basic medical sciences, Weifang medical university, Weifang, China

Animal behavior is organized into nested temporal patterns spanning multiple timescales. This behavior hierarchy is believed to arise from a hierarchical neural architecture: neurons near the top of the hierarchy are involved in planning, selecting, initiating, and maintaining motor programs while those near the bottom of the hierarchy act in concert to produce fine spatiotemporal motor activity. In *Caenorhabditis elegans*, behavior on a long timescale emerges from ordered and flexible transitions between different behavioral states, such as forward movement, reversal, and turn. On a short timescale, different parts of the animal body coordinate fast rhythmic bending sequences to produce directional movements. Here, we show SAA, a class of interneurons that enable cross-communication between dorsal and ventral head motor neurons, play a dual role in shaping behavioral dynamics on different timescales. On the short timescale, SAA regulate and stabilize rhythmic bending activity during forward movements. On the long timescale, the same neurons suppress spontaneous reversals and facilitate reversal termination by inhibiting RIM, an integrating neuron that helps sustain a behavioral state. These results suggest that feedback from a lower-level cell assembly to a higher-level command center is essential for bridging behavioral dynamics at different levels.

*Equal contribution

Correspondence: *xutq@ustc.edu.cn; qwen@ustc.edu.cn*

1 Introduction

In his book *The Study of Instinct*, Tinbergen proposed that animal behavior is a hierarchical organization of muscle activity patterns (1). Nest-building in stickleback, for example, is composed of a series of behaviors - like digging, testing materials, boring, and gluing - each of which can be subdivided into finer actions (on page 133-134, (1)). The nested structures across multiple timescales is the basis of behavioral hierarchy, where a behavioral module spanning a longer timescale stays near the top of the hierarchy. This theory has been elaborated and tested in classic ethological studies (2–4) and more recently by modern machine learning approaches (5–10). In particular, an unbiased method to classify behaviors and to quantify their relationships reveals a remarkable tree-like structure among all observable behavioral motifs in *Drosophila* (7).

The behavioral hierarchy is believed to stem from a hierarchical neural architecture of movement control (11–14): the neural code that represents a specific behavioral state is sparse and organized centrally while the neural representation that contributes to muscle synergy is distributed towards the periphery with increasingly dense and fast dynamics (15). Studies from several animal models appear to support this view. During zebra finch singing, a projection neuron in a premotor nucleus HVC generates sparse and short burst of spikes reliably at one precise moment in the entire song sequence (16, 17), while neurons in the downstream nucleus RA, which project to motor neurons to control syrinx, exhibit dense and variable firing (18). The foraging state in larval zebrafish, during which the animal suppresses swimming and promotes hunting, is represented by persistent activity in a sparse neural population in dorsal raphe (19). The hunting behavior, which is composed of rapid eye convergence and body J-turn, is represented by fast brain-wide activity across many midbrain and hindbrain areas (20). The attacking state in mouse is represented by slowly-varying population neural activity in a nucleus VMHv in hypothalamus, while sequential actions that entail faster dynamics are encoded by different neuron groups in a downstream nucleus MPOA (21).

The neural mechanisms underlying nested temporal patterns in naturalistic behavior, however, are poorly understood. The nematode *Caenorhabditis elegans* offers an opportunity to develop a deep understanding of the hierarchy problem, for the neural basis of worm behavior on different timescales has been studied in great detail (22–32). Let us use the foraging behavior as an example.

- At the top level, the *C. elegans* exploratory behavior exhibits two different strategies: local search (dwelling) after the animals are removed from food and global dispersal (roaming) after prolonged food deprivation (24). Two groups of neurons, NSM/HSN and PVP/AVB, which release serotonin and the neuropeptide PDF respectively, were shown to play opposing roles in modulating the dwelling and roaming state (33).

- At the middle level, *C. elegans* locomotion consists of forward movement, reversal, and turn. Local search is associated with a higher frequency of reversals and turns, while global dispersal promotes forward movements and inhibits reversals. Recent populational calcium imaging of immobilized and freely-behaving animals revealed that persistent activities in different groups of interneurons represent distinct motor states (29, 34, 35). For example, AVB/AIY/RIB exhibit elevated calcium activity during forward movements, while AVA/RIM/AIB exhibit elevated activity during reversal. The ordered and flexible sequential transitions between behaviors are controlled by both excitatory and inhibitory interactions between cell assemblies and a winner-take-all strategy for action selection (36–39).

- At the bottom level, directional movements require fast rhythmic bending waves propagating along the worm body. Forward movement in *C. elegans* is driven by B-type motor neurons and head motor neurons while reversal is driven by A-type motor neurons. Descending inputs from AVB, for example, are critical for triggering rhythmic activity in mid-body B-type motor neurons (30, 40). During reversal, AVA promotes rhythmic activity in A-type motor neurons (26, 38), while AIB/RIM inhibit SMD motor neurons to suppress head movements (13, 41).

The mounting experimental evidence suggests a scheme (Fig. 1) for organizing behavior across timescales: neural activity at each level along the hierarchy can have its intrinsic timescale, determined by the biophysical properties of neurons, the interactions between neurons within the same group, as well as the influence of neuromodulators. Feedforward inputs from top to bottom layers are primarily involved in selecting and gating diverse temporal patterns.

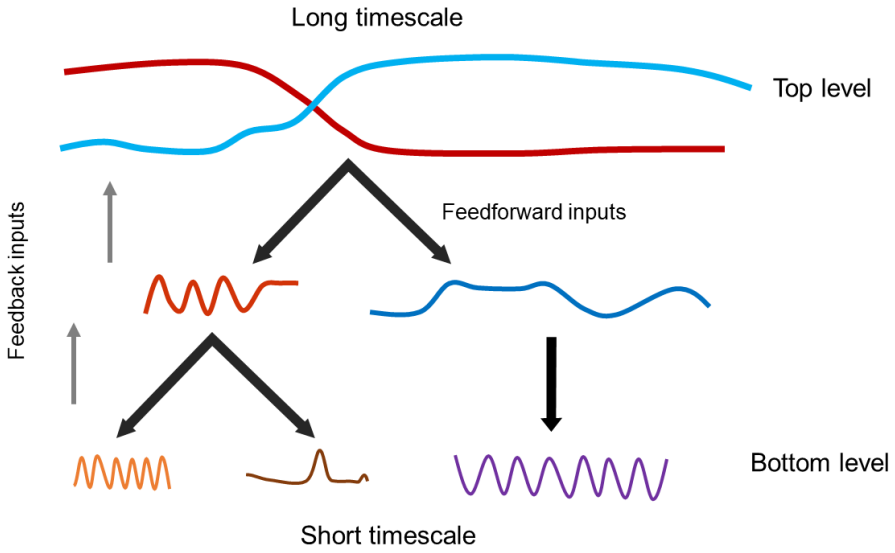

Figure 1. A scheme for organizing behaviors across different timescales.

Here we show that a class of interneurons SAA within the *C. elegans* head motor circuit play a dual role in shaping the timescales of low-level and high-level behavior dynamics. SAA make numerous connections with dorsal and ventral head motor neurons SMB/SMD/RMD, either by gap junctions or chemical synapses. We demonstrate that, on the short timescale, SAA regulate head bending kinematics and coordinate undulatory wave propagation during forward movements. Remarkably, on the long timescale, we find that feedback inhibition from SAA to RIM, an integrating neuron in the motor state control center, facilitates reversal termination and impacts stochastic transitions between motor states. The feedback from a lower-level to a higher-level circuitry (Fig. 1) *complements voluntary control* that uses a strict top-down strategy; and we argue that the presence of loops in a *pyramid-like* architecture (2) provides a more efficient and robust way to control behavior.

2 Results

2.1 SAA regulate and stabilize fast kinematics in forward locomotion

The *C. elegans* connectome (42, 43) indicates that SAA play a special role in the head motor circuit. SAA represent four interneurons that make reciprocal connections, either by electrical synapses or chemical synapses, with three classes of head motor neurons, SMB/SMD/RMD. For example, each of the four SMB motor neurons sends synapses to SAA, and they in turn make gap junctions with the SMB neurons that innervate muscles on the opposite side (Fig. 2A). This circuit motif allows for contra-lateral communication between SMBV and SMBD, which are not directly connected with each other.

To determine the functional contribution of SAA to head motor activity and *C. elegans* locomotion, we generated transgenic animals (P*lad-2*::Cre; P*lim-4*::loxP::PH-miniSOG) that enable optogenetic ablation of SAA neurons specifically (Methods). The kinematics of worm bending activity during forward movements in a viscous solution ($\eta = 800$ mPa·s) can be visualized by a curvature kymograph: in a control animal, each body segment alternated between positive (red) and negative (blue) curvature, and the bands of curvature propagated regularly from the head to the tail (head = 0; tail = 1) (Fig. 2B). In an SAA-ablated animal, the curvature bands appeared wider, and one found that the undulation frequency (Fig. 2F, Fig. S1B) as well as the speed of locomotion (Fig. 2E, Fig. S1A) were significantly reduced, while the overall bending amplitude became significantly increased (Fig. 2D).

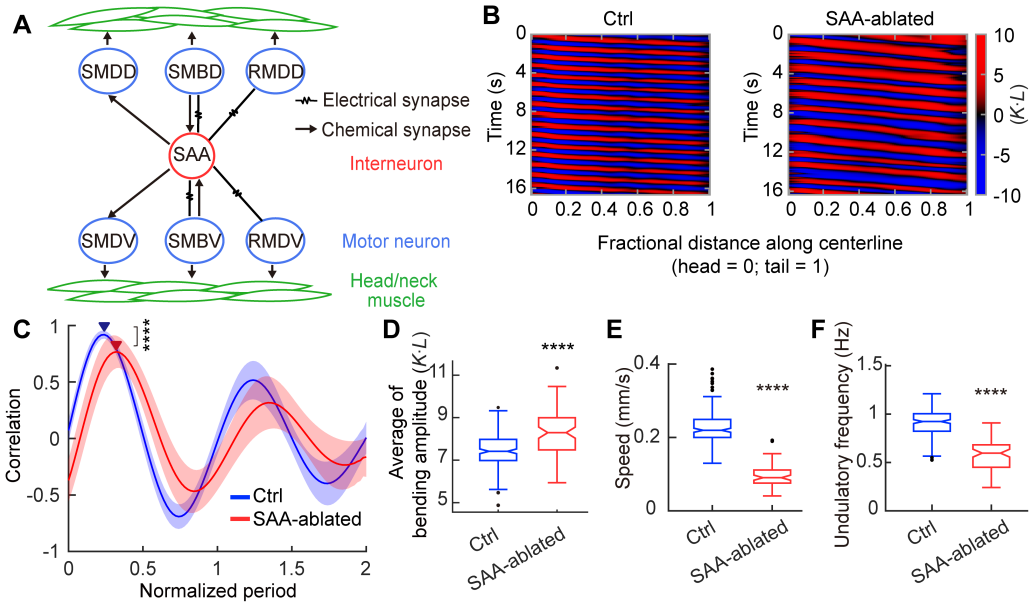

Figure 2. SAA neurons modulate kinematics in forward locomotion. A. Schematics of the circuit motif between SAA and head motor neurons. **B.** Representative curvature kymographs of control and SAA-ablated animals during forward movements. Body curvature was normalized by the worm body length L into a dimensionless unit $\kappa \cdot L$. **C.** Cross correlation of head curvature and body curvature over 2 periods of body undulation in control and SAA-ablated animals. To allow for a better comparison of propagation efficiency of bending amplitude across different trials, x-axis (time) was normalized by the average undulation period within a trial (a forward run). Blue curve: correlation (averaged over different trials after time normalization) in control group; red curve: correlation in SAA-ablated animals. Shaded areas on the two curves represent SD. Triangles indicate maximum correlation: Ctrl, 0.92 $\pm$ 0.03 (mean $\pm$ SD); SAA-ablated, 0.75 $\pm$ 0.23 (mean $\pm$ SD). ****P < 0.0001, Mann–Whitney U test. Ctrl: n = 164, 11 animals, SAA-ablated: n = 68, 22 animals. **D-F.** Whole-body bending amplitude (Methods), forward movement velocity, as well as undulation frequency in control and SAA-ablated animals. Experiments were conducted in 25% dextran solution. ****P < 0.0001, Black dots are outliers. Ctrl: n = 198, 11 animals; SAA-ablated: n = 80, 22 animals. Control group represents wild-type N2 strain; SAA-ablated group represents transgenic animals (P*lad-2*::Cre; P*lim-4*::loxP::PH-miniSOG).

Notably, the forward movements on the short timescale also appeared more irregular in SAA-ablated animals (Fig. 2B). The period of undulation varied significantly from time to time and exhibited a broader distribution (Fig. S1D). The cross correlation $C(\tau)$ between the head bending curvature and the midbody (fractional distance = 0.5, Fig. 2B) bending curvature (Methods) exhibited larger trial-to-trial variability (Fig. 2C, Fig. S1E). The spatiotemporal correlation of bending activity also suggests that the dynamic motion of an entire animal can be described by a small number of collective variables using Principal Component Analysis (25), and the time evolution

of worm behavior can be recapitulated by a trajectory in a low-dimensional phase space ((44) and Methods). A typical phase trajectory of a control animal appeared circular (Fig. 3D), indicating regular periodic motion; the phase trajectory of an SAA-ablated animal, however, was broadly extended (Fig. 3E). By examining the density of phase trajectories across trials and animals (Fig. 3A,B), we found that the motions of control animals were confined in a region resembling a torus while those of SAA-ablated animals were more broadly dispersed in the phase space (Fig. 3C). Taken together, these data suggest that SAA play an important role in modulating different aspects of bending kinematics as well as in stabilizing the dynamics of coordinated rhythmic motion.

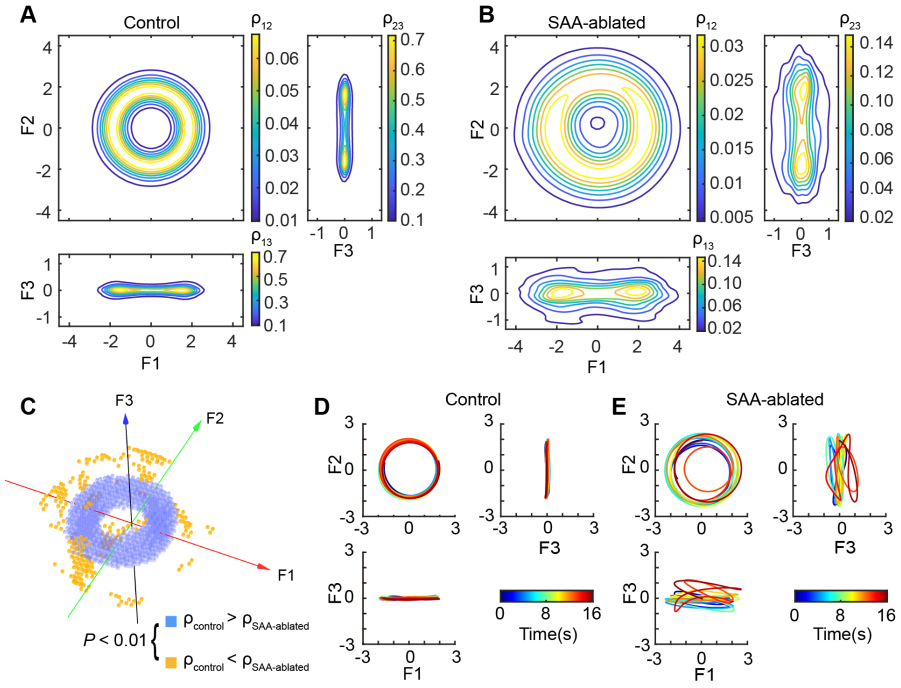

Figure 3. SAA stabilize rhythmic motion in forward movements. A. Density of trajectories embedded in 3-dimensional phase space during forward movements of control animals. Each of the three sub-panels represents a density projection onto a plane spanned by two orthogonal directions. **B.** Similar as **A**, but for SAA-ablated animals. **C.** Local density differences between **A** and **B** was visualized by a voxelgram (Methods). **D,E.** Time evolution of a phase trajectory in a control animal (**D**) and an SAA-ablated animal (**E**). Time is color-coded on the phase curves. Experiments in this figure were conducted in 25% dextran solution. Ctrl: n = 198, 11 animals; SAA-ablated: n = 80, 16 animals.

2.2 Impact of SAA on the long timescale locomotory behavior

Interestingly, we found that in SAA-ablated animals, the duration of a forward run significantly *decreased* (Fig. S2A-C), while the duration of a reversal significantly *increased* (Fig. S2D-F). As animals were swimming in a viscous solution in these experiments, we asked whether a similar observation may be identified in crawling animals. Specifically, we monitored the crawling behavior of *C. elegans* on an empty agar pad after the animal was removed from food for about 15 minutes, corresponding to the global dispersion state (33). Compared to control animals, SAA-ablated animals moved slower (Fig. S3C) and explored a much smaller territory in a similar amount of time (Fig. 4A and note the scale difference). The overall changes of short timescale kinematics were qualitatively similar to those of swimming animals (Fig. S3). On the long timescale, the cumulative density function (cdf) curve of forward run duration shifted upwards in SAA-ablated animals (Fig. 4C), consistent with a shorter run duration observed in the swimming condition (Fig. 4B and Fig. S2A). The mean spontaneous reversal duration of SAA-ablated and control animals were not statistically different (Fig. 4D), yet the cdf curves exhibited an interesting difference (Fig. 4E), suggesting that during crawling, SAA-ablated animals made extra very short (< 3 s) spontaneous reversals (P = 0.002, two side permutation t-test) as well as a few very long ones.

A shorter forward run duration (Fig. 4B-C) indicates that SAA-ablated animals made more frequent transitions to other motor states. Indeed, the frequency of reversals increased (Fig. 4G); the percentage of recording time during which animals spent on reversals or pauses significantly increased (Fig. 4F, P < 10^{-8}, χ^2 test). Consistent with this observation, during optogenetic inhibition of SAA (P*lim-4*::loxP::Arch;P*Lad-2*::Cre), animals were more likely to make reversals (Fig. 4H).

Not only did SAA affect long timescale spontaneous behaviors but also stimulus-triggered motor state transitions. Here we quantitatively characterized the escape responses in transgenic animals (P*mec-4*::Chrimson) induced by optogenetically activating mechanosensory neurons ALM/AVM (Fig. 4I). Ablation of SAA (P*lim-4*::PH-miniSOG, PH-miniSOG was also expressed in RIV and SMB neurons) led to longer reversals, suggesting that the ability to terminate reversals via backward-turn transitions was compromised (36).

2.3 Activation of SAA facilitates reversal termination

What is the neural basis underlying the observed long timescale behavioral changes in SAA-ablated animals? According to the *C.elegans* connectome, SAA make prominent chemical synapses with several interneurons (including RIM/AVA/AIB) that control backward movements (Fig. 5A). One possibility is that SAA activity can directly modulate motor state transitions through these interneurons. To test this hypothesis, we designed an experiment to optogenetically activate SAA during the reversal state. In order to avoid light spectra overlap, here we triggered an escape response by thermally stimulating the worm head for 1 second, followed by 7-second optogenetic activation of SAA (Fig. 5B, Methods). We constructed transgenic animals in which Chrimson was expressed specifically in SAA (P*lim-4*::loxP::Chrimson;P*Lad-2*::Cre) or in SAA/RIV/SMB neurons (P*lim-4*::Chrimson). Activation of SAA/RIV/SMB or SAA alone could rapidly terminate reversals: the *termination latency*, defined as the time between the onset of optogenetic stimulation and the end of a reversal, was significantly shorter than that in control animals (Fig. 5C and Methods). Consistent with the optogenetic experiment, we found that during the reversal-turn-forward transition, SAAD/SMB neurons exhibited an elevated calcium activity (Fig. 5E). Furthermore, stimulating SAA/RIV/SMB while blocking chemical synaptic transmission from these neurons (P*lim-4*::TeTx) prolonged the latency (Fig. 5D). Taken together, these results suggest that feedback synaptic inputs from a depolarized SAA unto the interneurons in the backward module facilitates reversal termination.

2.4 Inhibitory acetylcholine synaptic transmission promotes reversals termination

SAA are cholinergic neurons (45), and *C. elegans* nervous system possesses a family of acetylcholine-gated chloride (ACC) channels, and four putative subunits ACC-1 to ACC-4 have been identified (45, 46). We therefore ask whether these inhibitory acetylcholine receptors are involved in motor state transitions. We crossed transgenic animals (P*mec-4*::Chrimson) expressing Chrimson in mechanosensory neurons with ACC-deficient mutants: *acc-1(tm3268)*, *acc-2(tm3219)*, *acc-2(ok2216)*, *acc-3(tm3174)*, *acc-4(ok2371)*. Optogenetic activation of ALM and AVM could trigger prolonged reversals in these mutants (Fig. 6B). Interestingly, in two of the double mutants we tested (*acc-2(tm3219)*;*acc-3(tm3174)*, and *acc-3(tm3174)*;*acc-4(ok2371)*), the reversal duration was significantly longer than that in a single mutant (Fig. S4), indicating that these channel subunits act synergistically in the nervous system. Likewise, using the thermal and optogenetic stimulation protocol described in section 2.3, we found that the termination latency increased in ACC-deficient mutants (Fig. 6I and Fig. S5G,H,I).

2.5 RIM communicates with SAA to terminate reversals

Acetylcholine-gated chloride channels have a broad distribution within the *C. elegans* nervous system. Which neurons receive synaptic inputs from SAA to terminate reversal? Using GFP reporter lines, we focused on overlaps of acc expression patterns with those neurons known to encode backward motor states (Fig. 5A). We found that, intriguingly, all four ACC subunits are expressed in RIM (Fig. 6D-G), an integrating interneuron that plays a central role in motor state transitions (36, 37, 47, 48). A recent study (37) demonstrated that a depolarized RIM promotes spontaneous reversal whereas a hyperpolarized RIM suppresses reversal (also see Fig. S5F,J) by exploiting a combination of chemical and electrical synapses (Fig. 5A). The presence of four different types of acetylcholine-gated chloride channel subunits may coordinate to regulate RIM activity. Consistent with this notion, after restoring each of the 4 ACC channels expression specifically in RIM, we found that the duration of a reversal, triggered by an activation of mechanosensory neurons ALM/AVM, significantly reduced (Fig. 6C and Fig. S5B,C,D).

We further explored how synaptic inputs from SAA to RIM would shape the timescale of reversals. Using the thermal and optogenetic stimulation protocol, we found that restoring ACC subunit expression specifically in RIM significantly reduced the termination latency (Fig. 6I and Fig. S5G,H). In RIM-ablated animals, the termination latency, on the other hand, significantly increased (Fig. 6J). Finally, we directly observed a significant decrease in RIM calcium activity (P*tdc-1*:GCaMP6; P*tdc-1*:ChR2) immediately after optogenetic activation of SAA. As a control, we co-expressed channelrhodopsin (ChR2) in RIM to ensure that the neuron would be in a depolarized state during calcium imaging (Fig. 6K). Taken together, these experiments suggest that cholinergic synaptic inhibition from SAA to RIM contributes to reversal termination and promotes forward movements.

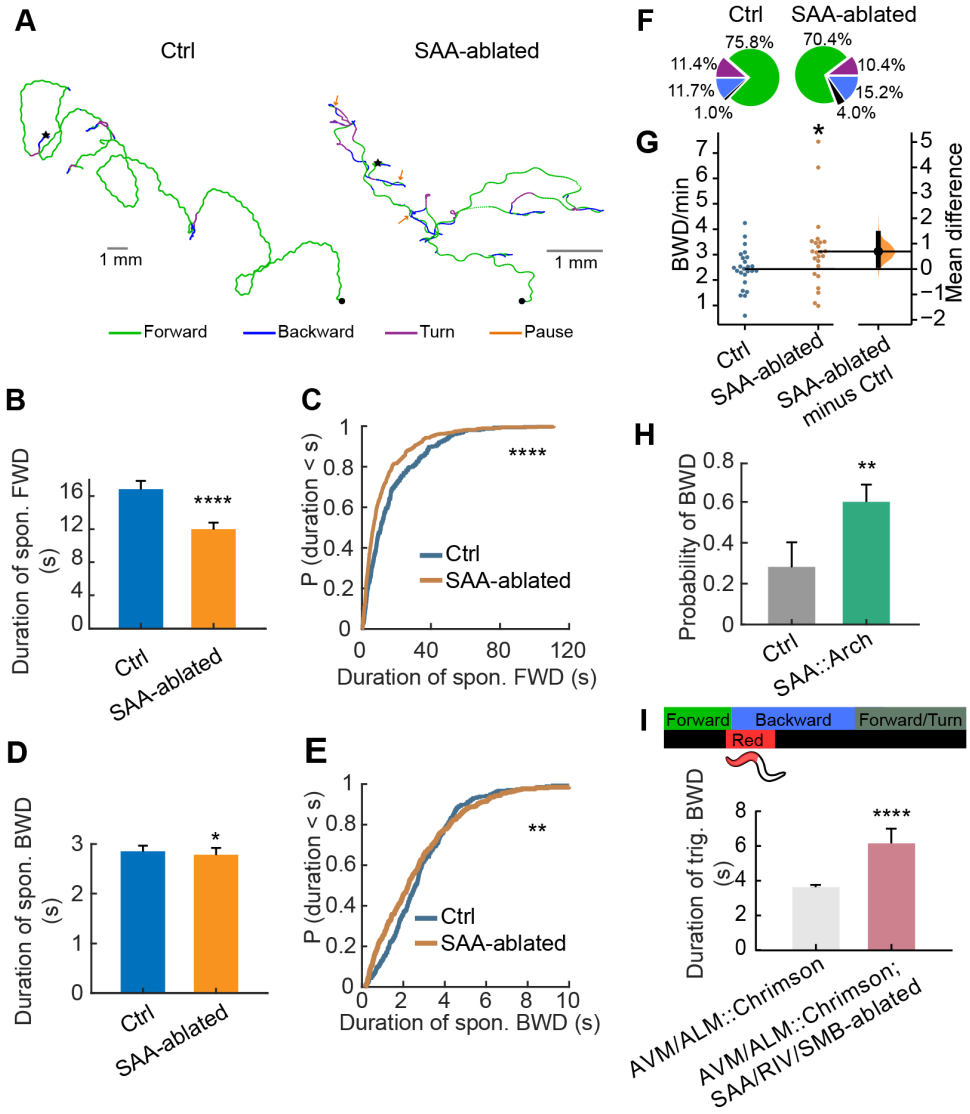

Figure 4. Impact of SAA on the long timescale crawling behaviors. A. Representative crawling trajectories of a control and an SAA-ablated animal. Different motor states are color coded, and arrows indicate pause state. Each worm was recorded for about 5 minutes. **B.** Mean duration of spontaneous forward runs in control and SAA-ablated animals. ****P < 0.0001, Mann–Whitney U test. Error bars represent SEM. **C.** Cumulative distributions of forward run length. Related to **B**. ****P < 0.0001, two-sample Kolmogorov–Smirnov test. Ctrl: n = 303; SAA-ablated: n = 398. **D.** Mean duration of spontaneous reversals in control and SAA-ablated animals. Error bars represent SEM. **E.** Cumulative distributions of reversal length. Related to **D**. **P < 0.01, two-sample Kolmogorov–Smirnov test. Ctrl: n = 276; SAA-ablated: n = 373. **F.** The percentage of time spent on forward movements, reversals, turns, or pauses. **G.** Gardner–Altman plots that display the effect sizes of reversal frequency in SAA-ablated and control animals. The black dot represents the mean difference. The 95% confidence interval of mean difference is illustrated by the black vertical line. The curve indicates the resampled distribution of mean difference. Data was aligned with the mean of control group. *P < 0.05, Mann–Whitney U test. **B**-**G**, Ctrl: 25 animals; SAA-ablated: 24 animals. **H.** The probability of eliciting a spontaneous reversal when SAA were optogenetically inhibited for 7 s by a green laser. The interval between optogenetic manipulations was > 45 s. Control group was fed with OP50 without all-trans-retinal. **P < 0.01, χ^2 test. Error bars represent 95% binomial proportion confidence interval. Ctrl: n = 39, 7 animals; SAA::Arch: n = 85, 18 animals. **I.** Top: schematic experimental procedure for triggering escape responses by activating AVM/ALM (P*mec-4*::Chrimson). The anterior half of an animal body was illuminated by 1.5 s red light during a forward movement. Bottom: duration of ALM/AVM-triggered reversals in control and SAA-ablated animals. ****P < 0.0001, Mann–Whitney U test. Error bars represent SEM. AVM/ALM::Chrimson: n = 414, 61 animals; AVM/ALM::Chrimson;SAA/RIV/SMB ablated: n = 41, 8 animals.

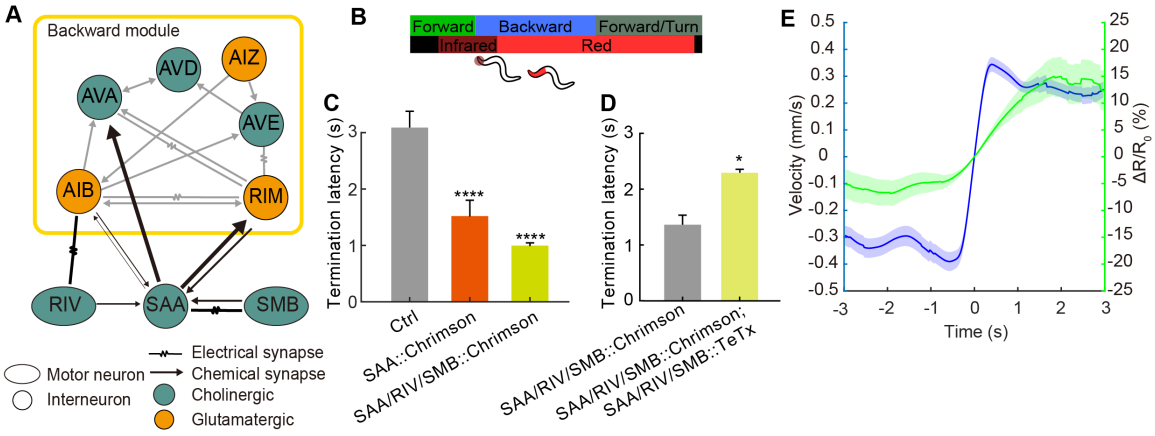

Figure 5. Activation of SAA facilitates reversal termination. A. The neuronal circuit bridging lower level head motor circuit and higher level command center. The synaptic convergence and divergence of SAA are proportional to the line width. For example, the number of synapses from SAA to RIM is ≈ 70 and the number of synapses from RIM to SAA is ≈ 30. **B.** Schematic experimental procedure for activation of SAA or SAA/RIV/SMB during thermally induced escape responses. Reversal was triggered by an infrared laser focusing on the worm head followed by optogenetic stimulation (red light). Related to **C**-**D**. **C.** Termination latency between the onset of optogenetic stimulation of SAA neurons or SAA/RIV/SMB neurons and the end of a reversal. ****P < 0.0001, compared with control group, Mann–Whitney U test with Bonferroni correction. Ctrl: n = 52, 10 animals; SAA::Chrimson: n = 36, 9 animals; SAA/RIV/SMB::Chrimson: n = 229, 53 animals. **D.** Similar as **C**, but in one group, the chemical synaptic transmission from SAA/RIV/SMB was blocked by an expression of tetanus toxin. *P < 0.05, compared with control group, Mann–Whitney U test. SAA/RIV/SMB::Chrimson: n = 65, 11 animals; SAA/RIV/SMB::Chrimson;SAA/RIV/SMB::TeTx: n = 60, 14 animals. **E.** Calcium imaging of SAAD/SMB near reversal-turn transition. t = 0 was aligned to reversal termination (i.e., velocity = 0 mm/s). Blue curve is the mean velocity of worm movements; green curve is the mean ratiometric calcium signal in SAAD/SMB neurons, plotted as $\Delta R/R_0 = (R(t) - R(t=0))/R(t=0)$. Shaded areas on the two curves represent SEM. n = 40, 13 animals.

3 Discussion

The neural basis of animal behavior, ranging from fast body movements to slow exploration-exploitation strategy, has been extensively studied in the literature (12, 13, 21, 33, 49–53). The behavioral hierarchy (Fig. 1) is an attractive conceptual framework to organize complex dynamics. By analogy, a dual hierarchy of timescales across visual pathway has been observed and modeled in a similar spirit (54), but with neural information flowing in the opposite direction. Whereas the transformation of sensory representation in a visual hierarchy has a clear circuit basis (55), the connection between the behavioral hierarchy and its neuronal circuit organization remains largely unclear. Here, we show that in *C. elegans*, the interneurons SAA, which are located at the lower level head motor circuit, bridge the short timescale dynamics that characterize the rhythmic bending activity and the long timescale dynamics that describe motor state transitions.

On the short timescale, we find that SAA modulate fast bending kinematics during forward movements, such as undulation frequency and amplitude (Fig. 2). SAA do not form neuromuscular junctions directly, but they make numerous chemical synapses and gap junctions with cholinergic head motor neurons, including SMB, SMD and RMD (Fig. 5A). How SAA mediate the activities in these motor neurons remains to be identified. The worm connectome (Fig. 2A) indicates that SAA enable cross-coupling between dorsal and ventral head motor neurons. This bilateral cross-coupled motif could be essential for stabilizing rhythmic motion by setting the correct phase difference between dorsal and ventral motor activities. In addition, SAA have processes extending anteriorly without pre-synaptic specializations, a feature that led White (43) to hypothesize that these processes have proprioceptive properties. One candidate for a potential mechanosensory channel is the TRP family (56), and TRP1 is known to express in SAA neurons (57). Previous works (30, 58, 59) suggest that when swimming in surroundings with different mechanical loads, *C. elegans* exhibited gait adaptation by exploiting local proprioceptive feedback. Consistent with this view, SAA-ablated animals exhibited a large variation of undulatory period when swimming in solutions with changing viscosities (Fig. S1C-D). Whether this observation results directly from a loss of proprioceptive signal, an impairment of the cross-coupled circuit, or both remain to be understood.

The impact of SAA on forward locomotion is not restricted to the head motor behavior; instead, the modulation is translated to the entire worm body (Fig. 3). Previous works (28, 30) showed that a directional proprioceptive

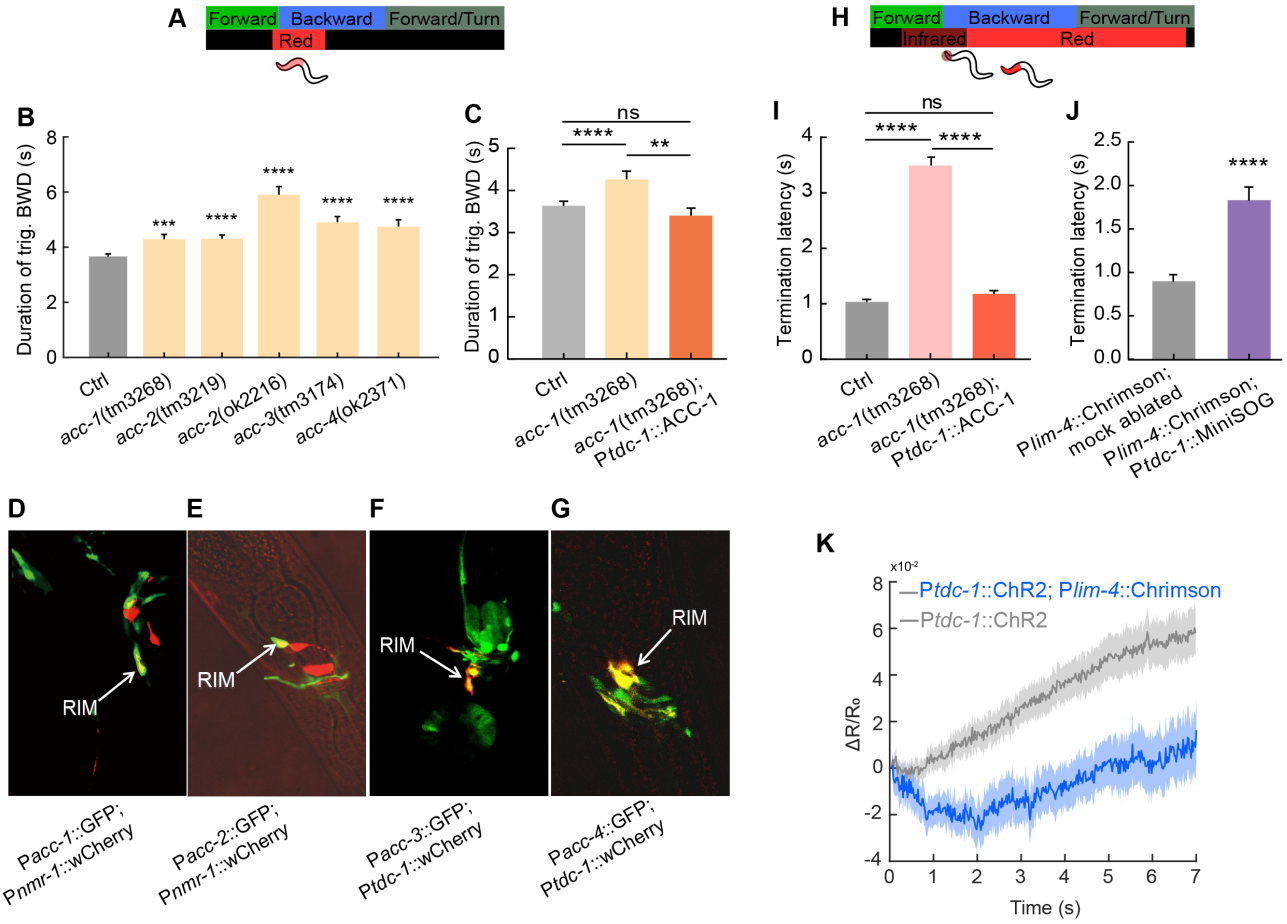

Figure 6. RIM communicates with SAA to terminate reversals via inhibitory acetylcholine synapses. **A.** Schematic experimental procedure for triggering escape responses (same as Fig. 4I). Optogenetic stimulation would activate AVM/ALM mechanosensory neurons. Related to **B**-**C**. **B.** Duration of ALM/AVM-triggered reversals in N2 (wild type) and ACC-deficient animals. Ctrl: n = 414, 61 animals; *acc-1(tm3268)*: n = 114, 16 animals; *acc-2(tm3219)*: n = 100, 10 animals; *acc-2(ok2216)*: n = 88, 12 animals; *acc-3(tm3174)*: n = 97, 11 animals; *acc-4(ok2371)*: n = 123, 16 animals. **C.** Duration of ALM/AVM-triggered reversal in N2, *acc-1* mutant, as well as animals in which ACC-1 was specifically restored in RIM. Ctrl: n = 414, 61 animals; *acc-1(tm3268)*: n = 114, 16 animals; *acc-1(tm3268)*;P*tdc-1::ACC-1*: n = 101, 16 animals. **D-G.** GFP reporter lines show a co-localization of acc-1, acc-2, acc-3, and acc-4 with RIM interneuron. **H.** Schematic procedure for dual thermal and optogenetic stimulation (same as Fig. 5B). Optogenetic stimulation would activate SAA/RIV/SMB neurons. Related to **I**-**J**. **I.** Termination latency in control, *acc-1* mutant, as well as animals in which ACC-1 was specifically restored in RIM. Ctrl: n = 229, 53 animals; *acc-1(tm3268)*: n = 96, 16 animals; *acc-1(tm3268)*;P*tdc-1::ACC-1*: n = 83, 15 animals. **J.** Termination latency in control and RIM ablated animals. P*lim-4*::Chrimson;mock ablated: n = 92, 25 animals; P*lim-4*::Chrimson;P*tdc-1*::MiniSOG: n = 96, 28 animals. All Statistical tests: **P<0.01, ***P<0.001, ****P < 0.0001, Mann–Whitney U test or Mann–Whitney U test with Bonferroni correction. Error bars represent SEM. **K.** Calcium dynamics of RIM neurons. Upon blue light excitation at t = 0, the GCaMP signal in RIM was being monitored. The co-expression of ChR2 in RIM would simultaneously depolarize the neuron during imaging, leading to a continuous increase of the calcium signal (grey). Activating RIM together with SAA/SMB/RIV led to a transient but significant decrease of calcium activity in RIM (blue) shortly after stimulation onset. Animals were immobilized in 10 % agarose pad with coverslip. P*tdc-1*::ChR2: n = 39, 7 animals; P*tdc-1*::ChR2;P*lim-4*::Chrimson: n = 21, 4 animals. Lines and shaded areas represent mean ± SEM.

coupling between B-type motor neurons enables rhythmic bending activity to propagate from head to tail. This mechanism can partially explain the global change of undulation dynamics in SAA-ablated animals (Fig. 2B and Fig. 3), but it cannot account for the change in the head-body coupling, manifested by a lower correlation between head and body curvature (Fig. 2C). One possibility is that SAA also receive inputs from B-type motor neurons that control body movements (42), and this type of functional coupling may improve the coherency of bending waves propagating from head to body.

On the long timescale, we find that SAA modulate motor state transitions by providing feedback inhibition to RIM, an integrating neuron that modulates the frequency and length of a reversal (37, 47, 48, 60). A bidirectional change in RIM activity can either promote or suppress the reversal state (37, 48). During stimulus triggered escape responses, the feedback inhibition is part of the winner-take-all strategy (36) that ensures a rapid and smooth transition from a reversal state to turn/forward movement state, accompanied by ramping calcium activity in SAAD (Fig. 5E). This inhibition is achieved by cholinergic synapses. Interestingly, we find that RIM expresses all 4 acetylcholine-gated chloride channel subunits and our data suggest that different ACC channel subunits do not act redundantly (Fig. S4). Here we postulate that a spatial combination of ACC subunits in the RIM cell body or neurites may contribute to fine-tuning the RIM membrane potential, and enable a precise control of motor state transitions.

The feedback inhibition from the lower-level head motor circuit to the higher-level control center also offers an efficient way to stabilize a behavioral state. In a navigational behavior, RIM and other interneurons in the backward module (Fig. 5A) are subject to noisy synaptic inputs from sensory neurons and recurrent connections. Continuous synaptic inhibition from SAA can hyperpolarize RIM and help sustain the global dispersion state (Fig. 4). Consistent with this notion, we found that inhibition or ablation of SAA led to an increase in the frequency of reversals (Fig. 4G-H); likewise, RIM-ablated animals also made more frequent transitions to reversals (Fig. S6). In *C. elegans*, bottom-up feedback connections (Fig. 1) enable robust behavioral control by complementing a strict top-down hierarchy. We believe this organization principle will find broad applications in many other motor systems.

4 Methods

4.1 Strains

Wild-type (N2), mutants, and transgenic animals were cultivated using standard methods. Specific promoter-driven expression of Chrimson, Arch, GCaMP6s, miniSOG or Tetanus Toxin was co-injected with P*lin-44*::GFP or P*unc-122*::GFP injection marker into N2 to generate transgenic animals. P*mec-4*::Chrimson (WEN1015) and P*lim-4*::Chrimson (WEN1009) were integrated by a UV illumination method and outcrossed 6X with N2 animals. The integrated lines were crossed with *acc-1*, *acc-2*, *acc-3* and *acc-4* mutants. Transgenic animals used in all optogenetic experiments were cultivated in the dark at 16 to 22 °C on NGM plates with *Escherichia coli* OP50 and all-trans retinal (ATR) for over 8 hours. We performed all experiments using young adult hermaphrodites.

4.2 Molecular biology

Standard molecular biology methods were used. Promoter such as P*lad-2*(2.1 kb), P*acc-1*(4.0 kb), P*acc-2*(2.0 kb), P*acc-3*(4.0 kb), and P*acc-4*(1.5 kb) was amplified by PCR from the genome of wild type animals.

4.3 Behavior recording

C. elegans were placed on 0.8% (wt/vol) M9 agar plate or immersed in dextran solution (5, 15, 25 % (wt/wt) dextran in M9 buffer). Before recording, worms were transferred to a sterile NGM plate to remove bacteria from the body surface and then transferred to the recording device: an agarose plate (0.8% (wt/vol) agarose in M9 buffer) or a chamber with dextran solution. The animals acclimatized themselves in the new environment for 10 to 15 minutes before being recorded freely for 5 to 10 minutes on a Nikon inverted microscope (Ti-U) with dark-field illumination.

4.4 Optogenetics

Experiments were performed on an inverted microscope (Ti-U, Nikon, Japan) under 10x magnification with dark-field illumination. Animals were placed on a 0.8% (wt/vol) M9 plate, and retained within the field of view of an imaging objective by a custom tracking system. Video sequences were captured by a Basler CMOS camera (aca 2000-340km), and the worm body centerline was extracted in real time. We used the MATLAB custom software (MathWorks, Natick, US) for post-processing behavioral data. We used the CoLBeRT system (61) to perform spatiotemporal optogenetic manipulation. For optogenetic activation of ALM/AVM neurons, we used a 635 nm solid-state laser with an intensity 4.6 mW/cm^2; in each trial, illumination lasted for 1.5 s.

4.5 Optogenetics ablation

Optogenetic ablation was carried out using transgenic strains, in which miniSOG was specifically expressed in neurons. We used mitochondrially targeted miniSOG (TOMM20-miniSOG) and a membrane-targeted miniSOG (PH-miniSOG) to induce cell death upon blue light stimulation. Well-fed L3/L4 animals were transferred to an unseeded NGM plate, and their movements were restricted within an area using a piece of filter paper with a hole in the center. The diameter of the restricted area was 0.5 cm, and the filter paper was soaked with 100 μM $CuCl_2$. Animals were illuminated for 15 (PH-miniSOG) or 30 (TOMM20-miniSOG) minutes with blue LED (M470L3-C5; Thorlabs) with an intensity of 133 mW/cm^2. The temporal sequence consists of 0.5/1.5 s on/off pulses.

4.6 Thermally induced escape responses and optogenetics

To trigger an escape response, we used a thermal stimulus and illuminated the head of a worm with a focused infrared laser (1480 nm, 5 mW/mm^2). Animals responded with reversals to avoid the thermal stimulus. To achieve sequential light activation, we used custom-written LabVIEW (National Instruments, US) scripts to control the diaphragm shutters (GCI 7102M, Daheng Optics, China) along the optical path. The 1 s infrared light stimulation (to trigger escape response) was followed by red (635 nm, 8.4 mW/cm^2) or green light (561 nm, 16 mW/mm^2) with a duration of 7 s to activate SAA/RIV/SMB neurons or inhibit RIM interneuron.

4.7 Calcium imaging

Calcium imaging was conducted on worms expressing GCaMP6s and wCherry in the same neurons. The calcium dynamics were calculated as a ratiometric change. We imaged SAAD and SMB neurons in animals crawling on a 2% (wt/vol) M9 agar plate (Fig. 5E) during a reversal-turn-forward transition. Reversals were triggered by an infrared laser (section 4.6) during a forward movement. To image calcium activity in RIM while simultaneously activating SAA (Fig. 6K), we synchronized blue light (488 nm) and green light (561 nm) excitation. Worms were immobilized by a high concentration agarose pad [10% (wt/vol)]. Illumination lasted for 7 s and the inter-activation interval was > 45 s. Green and red-light emission signals were collected by a Nikon Plan Apo 10X objective and separated by an optical splitter device (OptoSplit II, Cairn-Research, UK), each of which was then projected onto one-half of an sCMOS sensor (Zyla 4.2, Andor, UK). Neurons of interest were automatically identified using custom-written MATLAB scripts.

4.8 Statistical test

All statistical tests were described in the figure legends, including methods, error bars, number of trials and animals, as well as p values. We applied Mann–Whitney U test, χ^2 test to determine the significance of difference between groups, and Kolmogorov-Smirnov test to compare probability distributions. All multiple comparisons were adjusted using Bonferroni correction. We performed χ^2 test using Excel and all other analyses using MATLAB.

4.9 Kinematic analysis of locomotion

Recorded videos and the corresponding yaml files were first processed to identify motor states (forward run, reversal, pause and turn). The timestamp, stage position and the centerline of a worm were extracted using custom-written MATLAB scripts. To extract the bending curvature of an animal shown in Fig. 2, the worm centerline was first divided into $N = 100$ segments and the orientation of each segment, $\theta(s), s = 1, 2, \ldots, N$, was computed. The curvature $\kappa(s) = \Delta\theta(s)/\Delta s$ was calculated and then normalized into a dimensionless unit $\kappa \cdot L$, where L is the body length. A spatiotemporal filtering was carried out to obtain a smoothed version of $\kappa(s,t)$ for further analysis.

To quantify the correlation between head and body bending dynamics, we first computed a mean head/neck curvature defined as $\kappa_h(t) = \frac{1}{10}\sum_{s=15}^{s=24}\kappa(s,t)$, and a mean midbody curvature $\kappa_b(t) = \frac{1}{10}\sum_{s=45}^{s=54}\kappa(s,t)$. The cross correlation between head and body curvature with a time delay τ was computed using the standard formula

$$C(\tau) = \frac{\langle(\kappa_h(t) - \bar{\kappa}_h)(\kappa_b(t+\tau) - \bar{\kappa}_b)\rangle}{\sqrt{\langle(\kappa_h(t) - \bar{\kappa}_h)^2\rangle\langle(\kappa_b(t) - \bar{\kappa}_b)^2\rangle}}, \quad \textbf{(1)}$$

where $\bar{\kappa}_b$ and $\bar{\kappa}_h$ are mean head curvature and midbody curvature respectively, and $\langle ... \rangle$ denotes an average over the duration of a trial.

To quantify the whole-body bending amplitude, we first calculated the SD of curvature at a body segment

$$\sigma_\kappa(s) \equiv \sqrt{\langle(\kappa(s,t) - \bar{\kappa}(s))^2\rangle},$$

and we then averaged it over all segments $\bar{\sigma}_\kappa = \frac{1}{N}\sum_s \sigma_\kappa(s)$. We smoothed the local curvature at a middle body segment and used the local peak finding algorithm in MATLAB to identify local maxima/minima of curvature in a time sequence. Semi-period is the time difference between adjacent peak and trough.

4.10 Phase space reconstruction and analysis

To reduce the spatiotemporal bending activity of worm movements to a trajectory in a low-dimensional phase space, we followed the procedure introduced in (44). First, by performing a principal component analysis on the worm postures, we approximated the intrinsic coordinate of each body segment, represented by a time-evolving N-dimensional orientation vector $\vec{\theta}$, as a weighted sum of its leading principal components Θ (or eigenworms):

$$\vec{\theta}(t) \approx \sum_{i=1}^{D} a_i(t)\Theta_i, \tag{2}$$

where the coefficients $a_i(t) = \Theta_i^T\vec{\theta}(t)$, and we chose $D = 5$ such that the eigenworms captured more than 90% of the variance in worm posture data.

Next, we constructed a delay embedding matrix using the D-dimensional time coefficients (row vector) $\mathbf{a}(t) = [a_1, \ldots, a_D]$:

$$Y = \begin{bmatrix} \mathbf{a}(K) & \mathbf{a}(K-1) & \ldots & \mathbf{a}(1) \\ \mathbf{a}(K+1) & \mathbf{a}(K) & \ldots & \mathbf{a}(2) \\ \vdots & \vdots & \ddots & \vdots \\ \mathbf{a}(T) & \mathbf{a}(T-1) & \ldots & \mathbf{a}(T-K+1) \end{bmatrix},$$

where T is the number of time frames in a single trial (forward run), K is the history time window. Y thus is a $T-K+1 \times KD$ matrix. Here we chose K to be one half of the mean undulation period (44) in a single trial, and typically $T \gg KD$.

Finally, We performed singular value decomposition (SVD) of the Y matrix,

$$Y = \sum_{i=1}^{KD} \sigma_i \mathbf{u}_i \mathbf{v}_i^T, \tag{3}$$

where σ_i is the singular value in descending order and $\mathbf{v}_i$ is the corresponding KD-dimensional basis vector. By examining the covariance matrix Y^TY with eigenvalues σ_i^2, we found that with an embedding dimension $d = 3$, we could capture 94.1% variance in control animals and 89.6% variance in SAA-ablated animals during forward movements. We thus projected Y onto the first 3 basis vectors, namely $X_i = Y\mathbf{v}_i,\ i = 1,2,3$, where X_i is a $T-K+1$ column vector. The time evolution of $\vec{X}(t)$ was represented in Fig. 3D,E.

The spatial distribution of phase trajectories was analyzed using the kernel density method in MATLAB and shown in a contour plot (Fig. 3A,B). To compare the local density difference between control and SAA-ablated animals, we adopted an approach introduced in (62, 63), and used the kde.local.test function from the ks package in R to run a statistical test. Briefly, the phase space was first discretized into $50 \times 50 \times 50$ binning grid. Second, the local kernel density at a grid point was estimated and the 3D spatial density function was represented by a kernel density matrix. Finally, pairwise local density comparisons between two matrices were carried out with multiple comparison adjustment. The grid points that exhibited statistically significant ($P < 0.01$) differences were shown in Fig. 3C.

Supplementary information

S1 Supplementary figures. S1 comprises 6 supplementary figures.

ACKNOWLEDGEMENTS

We thank Zezhen Wang and Pinjie Li for helpful suggestions and preliminary analysis on the whole body bending kinematics. TX was supported by China Postdoctoral Science Foundation (project number 2020M682016) and QW was supported by Major International (Regional) Joint Research Project (32020103007).

Note added: When submitting this work, we became aware of Ref. (64), which partially overlap with this work.

5 Reference

1. Tinbergen, N. *The Study of Instinct*. The Study of Instinct. Clarendon Press/Oxford University Press, New York, NY, US, 1951.
2. Dawkins, R. Hierarchical organisation: A candidate principle for ethology. In *Growing Points in Ethology*. Cambridge U Press, Oxford, England, 1976.
3. Robertson, R. J. and Powers, W. T., editors. *Introduction to Modern Psychology: The Control-Theory View*. Introduction to Modern Psychology: The Control-Theory View. Control Systems Group, Gravel Switch, KY, US, 1990. ISBN 0-9624154-1-3 (Paperback).
4. Hölldobler, B. and Wilson, E. *The Ants*. Springer Berlin Heidelberg, 1998. ISBN 978-3-540-52092-4.
5. Botvinick, M. M., Niv, Y., and Barto, A. G. Hierarchically organized behavior and its neural foundations: A reinforcement learning perspective. *Cognition*, 113(3):262–280, Dec. 2009. doi: 10.1016/j.cognition.2008.08.011.
6. Berman, G. J., Choi, D. M., Bialek, W., and Shaevitz, J. W. Mapping the stereotyped behaviour of freely moving fruit flies. *Journal of The Royal Society Interface*, 11(99):20140672, Oct. 2014. doi: 10.1098/rsif.2014.0672.
7. Berman, G. J., Bialek, W., and Shaevitz, J. W. Predictability and hierarchy in *Drosophila* behavior. *Proceedings of the National Academy of Sciences*, 113(42):11943–11948, Oct. 2016. doi: 10.1073/pnas.1607601113.
8. Gomez-Marin, A., Stephens, G. J., and Brown, A. E. X. Hierarchical compression of *Caenorhabditis elegans* locomotion reveals phenotypic differences in the organization of behaviour. *Journal of The Royal Society Interface*, 13(121):20160466, Aug. 2016. doi: 10.1098/rsif.2016.0466.
9. Wiltschko, A. B., Johnson, M. J., Iurilli, G., Peterson, R. E., Katon, J. M., Pashkovski, S. L., Abraira, V. E., Adams, R. P., and Datta, S. R. Mapping Sub-Second Structure in Mouse Behavior. *Neuron*, 88(6):1121–1135, Dec. 2015. doi: 10.1016/j.neuron.2015.11.031.
10. Mathis, A., Mamidanna, P., Cury, K. M., Abe, T., Murthy, V. N., Mathis, M. W., and Bethge, M. DeepLabCut: Markerless pose estimation of user-defined body parts with deep learning. *Nature Neuroscience*, 21(9):1281–1289, Sept. 2018. doi: 10.1038/s41593-018-0209-y.
11. Ito, M. The control mechanism of Cerebellar motor system. In *The Neurosciences: Third Study Program*. The MIT Press, 1974.
12. Seeds, A. M., Ravbar, P., Chung, P., Hampel, S., Midgley, F. M., Jr, Mensh, B. D., and Simpson, J. H. A suppression hierarchy among competing motor programs drives sequential grooming in Drosophila. *eLife*, 3:e02951, Aug. 2014. doi: 10.7554/eLife.02951.
13. Kaplan, H. S., Salazar Thula, O., Khoss, N., and Zimmer, M. Nested Neuronal Dynamics Orchestrate a Behavioral Hierarchy across Timescales. *Neuron*, 105(3):562–576.e9, Feb. 2020. doi: 10.1016/j.neuron.2019.10.037.
14. Mazzucato, L. Neural mechanisms underlying the temporal organization of naturalistic animal behavior. *eLife*, 11:e76577, July 2022. doi: 10.7554/eLife.76577.
15. Meister, M. Learning, fast and slow. *Current opinion in neurobiology*, 75:102555, Aug. 2022. doi: 10.1016/j.conb.2022.102555.
16. Hahnloser, R. H., Kozhevnikov, A. A., and Fee, M. S. An ultra-sparse code underliesthe generation of neural sequences in a songbird. *Nature*, 419(6902):65–70, 2002.
17. Lynch, G. F., Okubo, T. S., Hanuschkin, A., Hahnloser, R. H., and Fee, M. S. Rhythmic Continuous-Time Coding in the Songbird Analog of Vocal Motor Cortex. *Neuron*, 90(4):877–892, May 2016. doi: 10.1016/j.neuron.2016.04.021.
18. Daliparthi, V. K., Tachibana, R. O., Cooper, B. G., Hahnloser, R. H., Kojima, S., Sober, S. J., and Roberts, T. F. Transitioning between preparatory and precisely sequenced neuronal activity in production of a skilled behavior. *eLife*, 8:e43732, June 2019. doi: 10.7554/eLife.43732.
19. Marques, J. C., Li, M., Schaak, D., Robson, D. N., and Li, J. M. Internal state dynamics shape brainwide activity and foraging behaviour. *Nature*, 577(7789):239–243, Jan. 2020. doi: 10.1038/s41586-019-1858-z.
20. Antinucci, P., Folgueira, M., and Bianco, I. H. Pretectal neurons control hunting behaviour. *eLife*, 8:e48114, Oct. 2019. doi: 10.7554/eLife.48114.
21. Nair, A., Karigo, T., Yang, B., Ganguli, S., Schnitzer, M. J., Linderman, S. W., Anderson, D. J., and Kennedy, A. An approximate line attractor in the hypothalamus encodes an aggressive state. *Cell*, 186(1):178–193.e15, Jan. 2023. doi: 10.1016/j.cell.2022.11.027.
22. Sawin, E. R., Ranganathan, R., and Horvitz, H. C. elegans Locomotory Rate Is Modulated by the Environment through a Dopaminergic Pathway and by Experience through a Serotonergic Pathway. *Neuron*, 26(3):619–631, June 2000. doi: 10.1016/S0896-6273(00)81199-X.
23. Tsalik, E. L. and Hobert, O. Functional mapping of neurons that control locomotory behavior inCaenorhabditis elegans. *Journal of Neurobiology*, 56(2):178–197, Aug. 2003. doi: 10.1002/neu.10245.
24. Gray, J. M., Hill, J. J., and Bargmann, C. I. A circuit for navigation in *Caenorhabditis elegans*. *Proceedings of the National Academy of Sciences*, 102(9):3184–3191, Mar. 2005. doi: 10.1073/pnas.0409009101.
25. Stephens, G. J., Johnson-Kerner, B., Bialek, W., and Ryu, W. S. Dimensionality and Dynamics in the Behavior of C. elegans. *PLOS Computational Biology*, 4(4):e1000028, 2008. doi: 10.1371/journal.pcbi.1000028.
26. Kawano, T., Po, M. D., Gao, S., Leung, G., Ryu, W. S., and Zhen, M. An Imbalancing Act: Gap Junctions Reduce the Backward Motor Circuit Activity to Bias C. elegans for Forward Locomotion. *Neuron*, 72(4):572–586, Nov. 2011. doi: 10.1016/j.neuron.2011.09.005.
27. Piggott, B. J., Liu, J., Feng, Z., Wescott, S. A., and Xu, X. Z. S. The Neural Circuits and Synaptic Mechanisms Underlying Motor Initiation in C. elegans. *Cell*, 147(4):922–933, Nov. 2011. doi: 10.1016/j.cell.2011.08.053.
28. Wen, Q., Po, M. D., Hulme, E., Chen, S., Liu, X., Kwok, S. W., Gershow, M., Leifer, A. M., Butler, V., Fang-Yen, C., Kawano, T., Schafer, W. R., Whitesides, G., Wyart, M., Chklovskii, D. B., Zhen, M., and Samuel, A. D. T. Proprioceptive coupling within motor neurons drives C. elegans forward locomotion. *Neuron*, 76(4):750–761, Nov. 2012. doi: 10.1016/j.neuron.2012.08.039.
29. Luo, L., Wen, Q., Ren, J., Hendricks, M., Gershow, M., Qin, Y., Greenwood, J., Soucy, E. R., Klein, M., Smith-Parker, H. K., Calvo, A. C., Colón-Ramos, D. A., Samuel, A. D. T., and Zhang, Y. Dynamic encoding of perception, memory, and movement

in a C. elegans chemotaxis circuit. *Neuron*, 82(5):1115–1128, June 2014. doi: 10.1016/j.neuron.2014.05.010.

30. Xu, T., Huo, J., Shao, S., Po, M., Kawano, T., Lu, Y., Wu, M., Zhen, M., and Wen, Q. Descending pathway facilitates undulatory wave propagation in Caenorhabditis elegans through gap junctions. *Proceedings of the National Academy of Sciences*, 115(19):201717022, 2018. doi: 10.1073/pnas.1717022115.
31. Kaplan, H. S., Salazar Thula, O., Khoss, N., and Zimmer, M. Nested Neuronal Dynamics Orchestrate a Behavioral Hierarchy across Timescales. *Neuron*, 105(3):562–576.e9, Feb. 2020. doi: 10.1016/j.neuron.2019.10.037.
32. Ji, N., Madan, G. K., Fabre, G. I., Dayan, A., Baker, C. M., Kramer, T. S., Nwabudike, I., and Flavell, S. W. A neural circuit for flexible control of persistent behavioral states. *eLife*, 10:e62889, Nov. 2021. doi: 10.7554/eLife.62889.
33. Flavell, S. W., Pokala, N., Macosko, E. Z., Albrecht, D. R., Larsch, J., and Bargmann, C. I. Serotonin and the neuropeptide PDF initiate and extend opposing behavioral states in C. elegans. *Cell*, 154(5):1023–1035, Aug. 2013. doi: 10.1016/j.cell.2013.08.001.
34. Kato, S., Kaplan, H. S., Schrödel, T., Skora, S., Lindsay, T. H., Yemini, E., Lockery, S., and Zimmer, M. Global Brain Dynamics Embed the Motor Command Sequence of Caenorhabditis elegans. *Cell*, 163(3):656–669, Oct. 2015. doi: 10.1016/j.cell.2015.09.034.
35. Hallinen, K. M., Dempsey, R., Scholz, M., Yu, X., Linder, A., Randi, F., Sharma, A. K., Shaevitz, J. W., and Leifer, A. M. Decoding locomotion from population neural activity in moving C. elegans. *eLife*, 10:e66135, July 2021. doi: 10.7554/eLife.66135.
36. Wang, Y., Zhang, X., Xin, Q., Hung, W., Florman, J., Huo, J., Xu, T., Xie, Y., Alkema, M. J., Zhen, M., and Wen, Q. Flexible motor sequence generation during stereotyped escape responses. *eLife*, 9:e56942, 2020. doi: 10.7554/elife.56942.
37. Sordillo, A. and Bargmann, C. I. Behavioral control by depolarized and hyperpolarized states of an integrating neuron. *eLife*, 10:e67723, Nov. 2021. doi: 10.7554/eLife.67723.
38. Meng, J., Ahamed, T., Yu, B., Hung, W., Mouridi, S. E., Wang, Z., Zhang, Y., Wen, Q., Boulin, T., Gao, S., and Zhen, M. A tonically active master neuron continuously modulates mutually exclusive motor states at two-time scales. *bioRxiv*, page 2022.04.06.487231, Jan. 2022. doi: 10.1101/2022.04.06.487231.
39. Chen, L., Liu, Y., Su, P., Hung, W., Li, H., Wang, Y., Yue, Z., Ge, M.-H., Wu, Z.-X., Zhang, Y., Fei, P., Chen, L.-M., Tao, L., Mao, H., Zhen, M., and Gao, S. Escape steering by cholecystokinin peptidergic signaling. *Cell Reports*, 38(6):110330, Feb. 2022. doi: 10.1016/j.celrep.2022.110330.
40. Fouad, A. D., Teng, S., Mark, J. R., Liu, A., Alvarez-Illera, P., Ji, H., Du, A., Bhirgoo, P. D., Cornblath, E., Guan, S. A., and Fang-Yen, C. Distributed rhythm generators underlie Caenorhabditis elegans forward locomotion. *eLife*, 7:e29913, Jan. 2018. doi: 10.7554/eLife.29913.
41. Pirri, J. K., McPherson, A. D., Donnelly, J. L., Francis, M. M., and Alkema, M. J. A Tyramine-Gated Chloride Channel Coordinates Distinct Motor Programs of a Caenorhabditis elegans Escape Response. *Neuron*, 62(4):526–538, May 2009. doi: 10.1016/j.neuron.2009.04.013.
42. White, J. G., Southgate, E., Thomson, J. N., and Brenner, S. The structure of the nervous system of the nematode Caenorhabditis elegans. *Philosophical transactions of the Royal Society of London. Series B, Biological sciences*, 314 (1165):1–340, Nov. 1986. doi: 10.1098/rstb.1986.0056.
43. White, J. Clues to basis of exploratory behaviour of the C. elegans snout from head somatotropy. *Philosophical Transactions of the Royal Society B: Biological Sciences*, 373(1758):20170367, Sept. 2018. doi: 10.1098/rstb.2017.0367.
44. Ahamed, T., Costa, A. C., and Stephens, G. J. Capturing the continuous complexity of behaviour in Caenorhabditis elegans. *Nature Physics*, 17(2):275–283, Feb. 2021. doi: 10.1038/s41567-020-01036-8.
45. Pereira, L., Kratsios, P., Serrano-Saiz, E., Sheftel, H., Mayo, A. E., Hall, D. H., White, J. G., LeBoeuf, B., Garcia, L. R., Alon, U., and Hobert, O. A cellular and regulatory map of the cholinergic nervous system of C. elegans. *eLife*, 4:e12432, 2015. doi: 10.7554/eLife.12432.
46. Putrenko, I., Zakikhani, M., and Dent, J. A. A family of acetylcholine-gated chloride channel subunits in Caenorhabditis elegans. *The Journal of Biological Chemistry*, 280(8):6392–6398, Feb. 2005. doi: 10.1074/jbc.M412644200.
47. Gordus, A., Pokala, N., Levy, S., Flavell, S. W., and Bargmann, C. I. Feedback from network states generates variability in a probabilistic olfactory circuit. *Cell*, 161(2):215–227, Apr. 2015. doi: 10.1016/j.cell.2015.02.018.
48. Ji, N., Venkatachalam, V., Rodgers, H. D., Hung, W., Kawano, T., Clark, C. M., Lim, M., Alkema, M. J., Zhen, M., and Samuel, A. D. Corollary discharge promotes a sustained motor state in a neural circuit for navigation. *eLife*, 10:e68848, Apr. 2021. doi: 10.7554/eLife.68848.
49. Fyhn, M., Molden, S., Witter, M. P., Moser, E. I., and Moser, M.-B. Spatial Representation in the Entorhinal Cortex. *Science*, 305(5688):1258–1264, Aug. 2004. doi: 10.1126/science.1099901.
50. Recanatesi, S., Pereira-Obilinovic, U., Murakami, M., Mainen, Z., and Mazzucato, L. Metastable attractors explain the variable timing of stable behavioral action sequences. *Neuron*, 110(1):139–153.e9, Jan. 2022. doi: 10.1016/j.neuron.2021.10.011.
51. Nakajima, T., Hosaka, R., and Mushiake, H. Complementary Roles of Primate Dorsal Premotor and Pre-Supplementary Motor Areas to the Control of Motor Sequences. *Journal of Neuroscience*, 42(36):6946–6965, Sept. 2022. doi: 10.1523/JNEUROSCI.2356-21.2022.
52. Liberti, W. A., Schmid, T. A., Forli, A., Snyder, M., and Yartsev, M. M. A stable hippocampal code in freely flying bats. *Nature*, 604(7904):98–103, Apr. 2022. doi: 10.1038/s41586-022-04560-0.
53. Berg, E. M., Mrowka, L., Bertuzzi, M., Madrid, D., Picton, L. D., and El Manira, A. Brainstem circuits encoding start, speed, and duration of swimming in adult zebrafish. *Neuron*, 111(3):372–386.e4, Feb. 2023. doi: 10.1016/j.neuron.2022.10.034.
54. Murray, J. D., Bernacchia, A., Freedman, D. J., Romo, R., Wallis, J. D., Cai, X., Padoa-Schioppa, C., Pasternak, T., Seo, H., Lee, D., and Wang, X.-J. A hierarchy of intrinsic timescales across primate cortex. *Nature Neuroscience*, 17(12):1661–1663, Dec. 2014. doi: 10.1038/nn.3862.
55. Felleman, D. J. and Van Essen, D. C. Distributed Hierarchical Processing in the Primate Cerebral Cortex. *Cerebral Cortex*, 1(1):1–47, Jan. 1991. doi: 10.1093/cercor/1.1.1-a.
56. Xiao, R. and Xu, X. S. C. elegans TRP channels. *Advances in experimental medicine and biology*, 704:323–339, 2011. doi: 10.1007/978-94-007-0265-3_18.
57. Kalogeropoulou, E. *Role of the SAA and SMB Neurons in Locomotion in the Nematode Caenorhabditis Elegans, with a*

Focus on Steering. Doctoral Thesis (Ph.D.), University of Leeds, University of Leeds, 2018.

58. Boyle, J. H., Berri, S., and Cohen, N. Gait Modulation in C. elegans: An Integrated Neuromechanical Model. *Frontiers in Computational Neuroscience*, 6:10, Mar. 2012. doi: 10.3389/fncom.2012.00010.
59. Ji, H., Fouad, A. D., Teng, S., Liu, A., Alvarez-Illera, P., Yao, B., Li, Z., and Fang-Yen, C. Phase response analyses support a relaxation oscillator model of locomotor rhythm generation in Caenorhabditis elegans. *eLife*, 10:e69905, Sept. 2021. doi: 10.7554/eLife.69905.
60. Guo, Z. V., Hart, A. C., and Ramanathan, S. Optical interrogation of neural circuits in Caenorhabditis elegans. *Nature Methods*, 6(12):891–896, Dec. 2009. doi: 10.1038/nmeth.1397.
61. Leifer, A. M., Fang-Yen, C., Gershow, M., Alkema, M. J., and Samuel, A. D. T. Optogenetic manipulation of neural activity in freely moving Caenorhabditis elegans. *Nature methods*, 8(2):147–152, Feb. 2011. doi: 10.1038/nmeth.1554.
62. Duong, T. **Ks** : Kernel Density Estimation and Kernel Discriminant Analysis for Multivariate Data in *R*. *Journal of Statistical Software*, 21(7), 2007. doi: 10.18637/jss.v021.i07.
63. Das, R., Lin, L.-C., Català-Castro, F., Malaiwong, N., Sanfeliu-Cerdán, N., Porta-de-la-Riva, M., Pidde, A., and Krieg, M. An asymmetric mechanical code ciphers curvature-dependent proprioceptor activity. *Science Advances*, 7(38):eabg4617, Sept. 2021. doi: 10.1126/sciadv.abg4617.
64. Kumar, S., Sharma, A. K., and Leifer, A. Inhibitory motor signals gate mechanosensory processing in C. elegans. *arXiv*, 2023. doi: 10.48550/ARXIV.2301.02709.

Supplementary figures (S1)

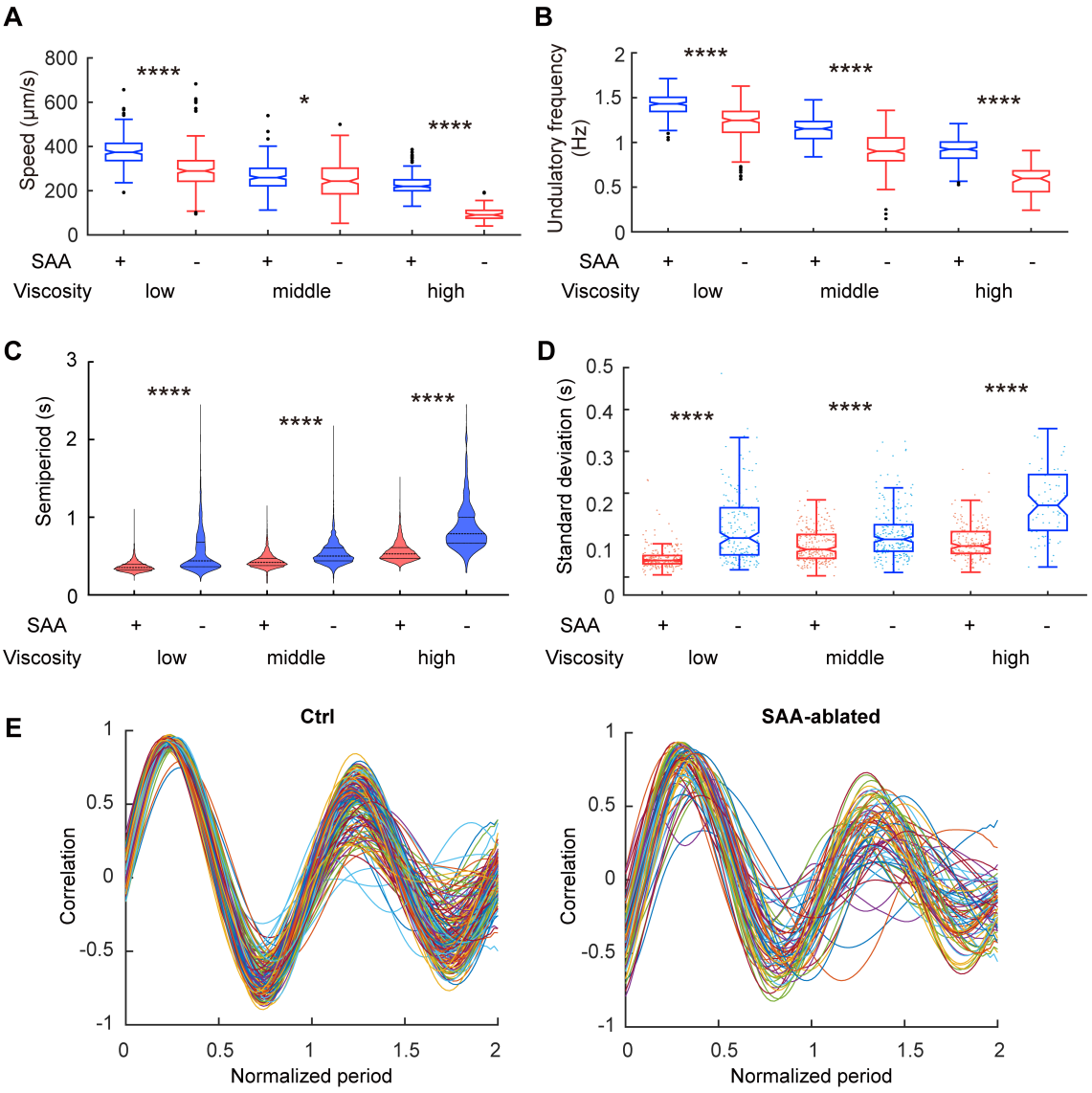

Figure S1. SAA contribute to stabilizing swimming kinematics. A-C. Velocity, undulation frequency, semi-period in control and SAA-ablated animals during forward locomotion in viscous solutions. **D.** Standard deviation of semi-period in control and SAA-ablated animals. Red and blue dots are standard deviations of each trial's semi-period. **A-D**: low, middle, or high viscosity represents 5% (9 mPa·s), 15 % (120 mPa·s), and 25% (800 mPa·s) dextran in M9 solution, respectively. *P < 0.05, ****P < 0.0001, Mann–Whitney U test with Bonferroni correction. Black dots are outliers. Control animals were wild type N2 strain. Ctrl, low viscosity: n = 233, 11 animals; Ctrl, middle viscosity: n = 239, 16 animals; Ctrl, high viscosity: n = 198, 11 animals; SAA-ablated, low viscosity: 190, 22 animals; SAA-ablated, middle viscosity: n = 224, 13 animals; SAA-ablated, high viscosity: n = 80, 16 animals. **E.** Cross correlation of head curvature and body curvature over 2 periods of body undulation in control and SAA-ablated animals swimming in 25% dextran solution. Same as Fig. 2C except that multicolor curves represent individual trials. Trial duration: Ctrl, 10.21 s ± 7.28 s (mean ± SD); SAA-ablated, 9.94 s ± 4.50 s (mean ± SD).

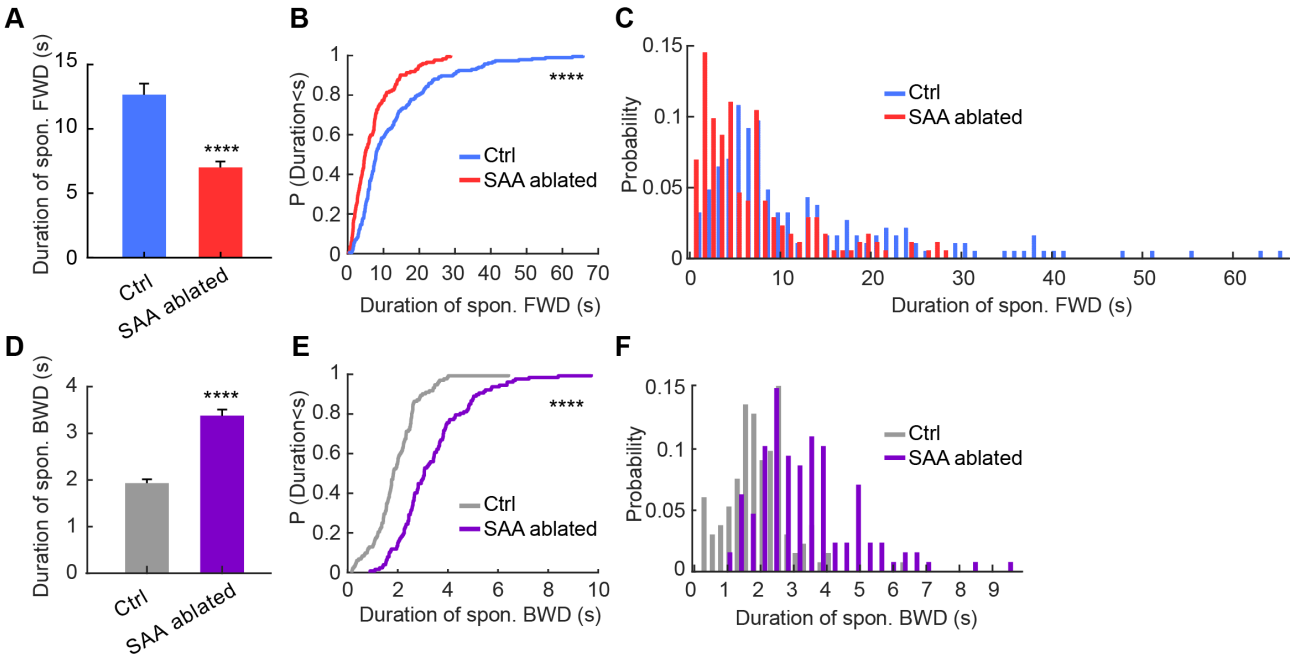

Figure S2. SAA contribute to organizing long timescale swimming behaviors. A. Mean duration of forward movements. ****P < 0.0001, Mann–Whitney U test. Error bars represent SEM. Ctrl: n = 185, 11 animals; SAA-ablated: n = 172, 16 animals. **B.** Cumulative distributions of forward run length. Related to **A**. ****P < 0.0001, two-sample Kolmogorov–Smirnov test. **C.** Probability distributions of forward run length. Related to **A**. **D.** Mean duration of spontaneous reversals. ****P < 0.0001, Mann–Whitney U test. Error bars represent SEM. Ctrl: n = 132, 11 animals; SAA-ablated: n = 127, 16 animals. **E.** Cumulative distributions of spontaneous reversal length. Related to **D**. ****P < 0.0001, two-sample Kolmogorov–Smirnov test. **F.** Probability distributions of reversal length. Related to **D**. All animals swam in a viscous solution (800 mPa·s).

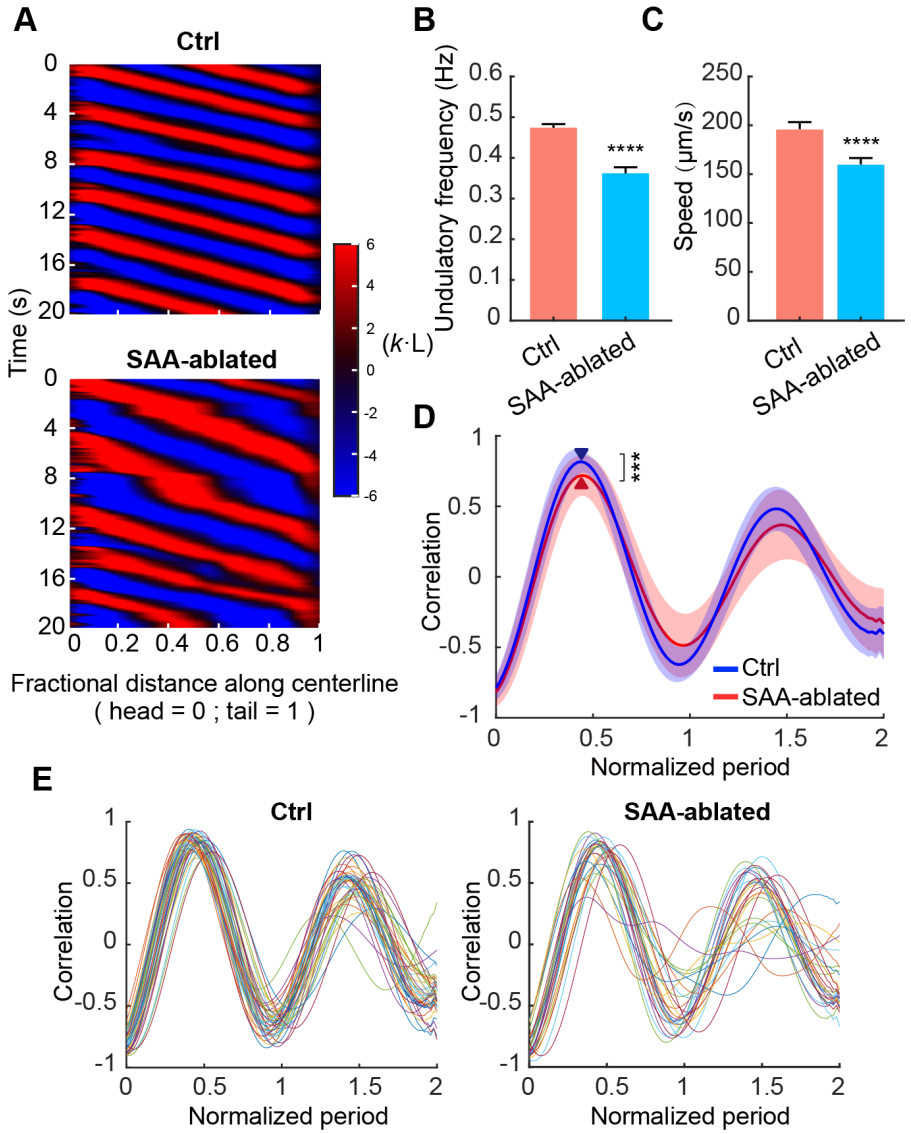

Figure S3. SAA contribute to organizing short timescale kinematics in crawling animals. A. Representative curvature kymographs of control and SAA-ablated animals during forward movements. Body curvature was normalized by the worm body length L into a dimensionless unit $\kappa \cdot L$. **B-C.** Undulation frequency and velocity in control and SAA-ablated animals during forward movements. ****P < 0.0001, Mann–Whitney U test. Ctrl: n = 51, 14 animals; SAA-ablated: n = 48, 11 animals. **D.** Cross correlation of head curvature and body curvature over 2 periods of body undulation in control and SAA-ablated animals, similar to Fig. 2C except that all animals crawled on agar pads. Triangles indicate maximum correlation: Ctrl, 0.85 $\pm$ 0.05 (mean $\pm$ SD); SAA-ablated, 0.76 $\pm$ 0.12 (mean $\pm$ SD). ***P < 0.001, Mann–Whitney U test. Ctrl: n = 41, 14 animals; SAA-ablated: n = 28, 11 animals.To allow for a better comparison of propagation efficiency of bending amplitude across different trials, x-axis (time) was normalized by the average undulation period within a trial. Multicolor traces represent individual trials with an undulation period 1.69 s $\pm$ 0.35 s (mean $\pm$ SD) in control group and 2.20 s $\pm$ 0.39 s (mean $\pm$ SD) in SAA-ablated group. **E.** Same as **D** except that multicolor curves represent individual trials.

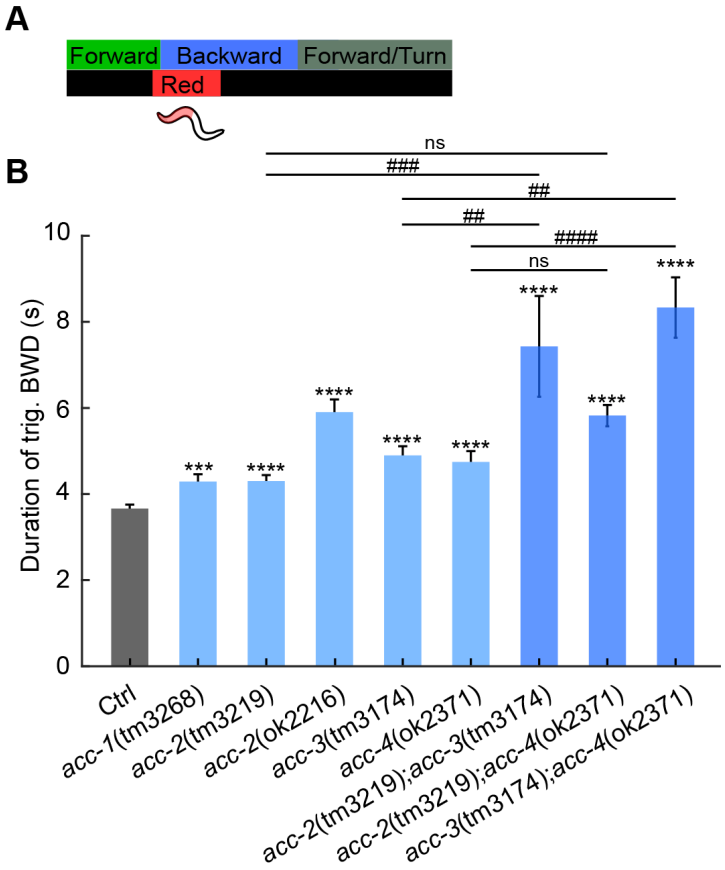

Figure S4. Acetylcholine-gated chloride channel subunits function synergistically to modulate reversal length during ALM/AVM-triggered escape responses. The duration of ALM/AVM-triggered reversals in a single *acc* mutant or a double mutant. ***P<0.001, ****P < 0.0001, compared with control; ##P<0.01, ###P<0.001, ####P<0.0001, compared between corresponding mutants; Mann–Whitney U test with with Bonferroni correction. Error bars represent SEM. Ctrl (N2): n = 414, 61 animals; *acc-1(tm3268)*: n = 114, 16 animals; *acc-2(tm3219)*: n = 100, 10 animals; *acc-2(ok2216)*: n = 88, 12 animals; *acc-3(tm3174)*: n = 97, 11 animals; *acc-4(ok2371)*: n = 123, 16 animals; *acc-2(tm3219)*; *acc-3(tm3174)*: n = 24, 4 animals; *acc-2(tm3219)*; *acc-4(ok2371)*: n = 134, 20 animals; *acc-3(tm3174)*; *acc-4(ok2371)*: n = 171, 30 animals.

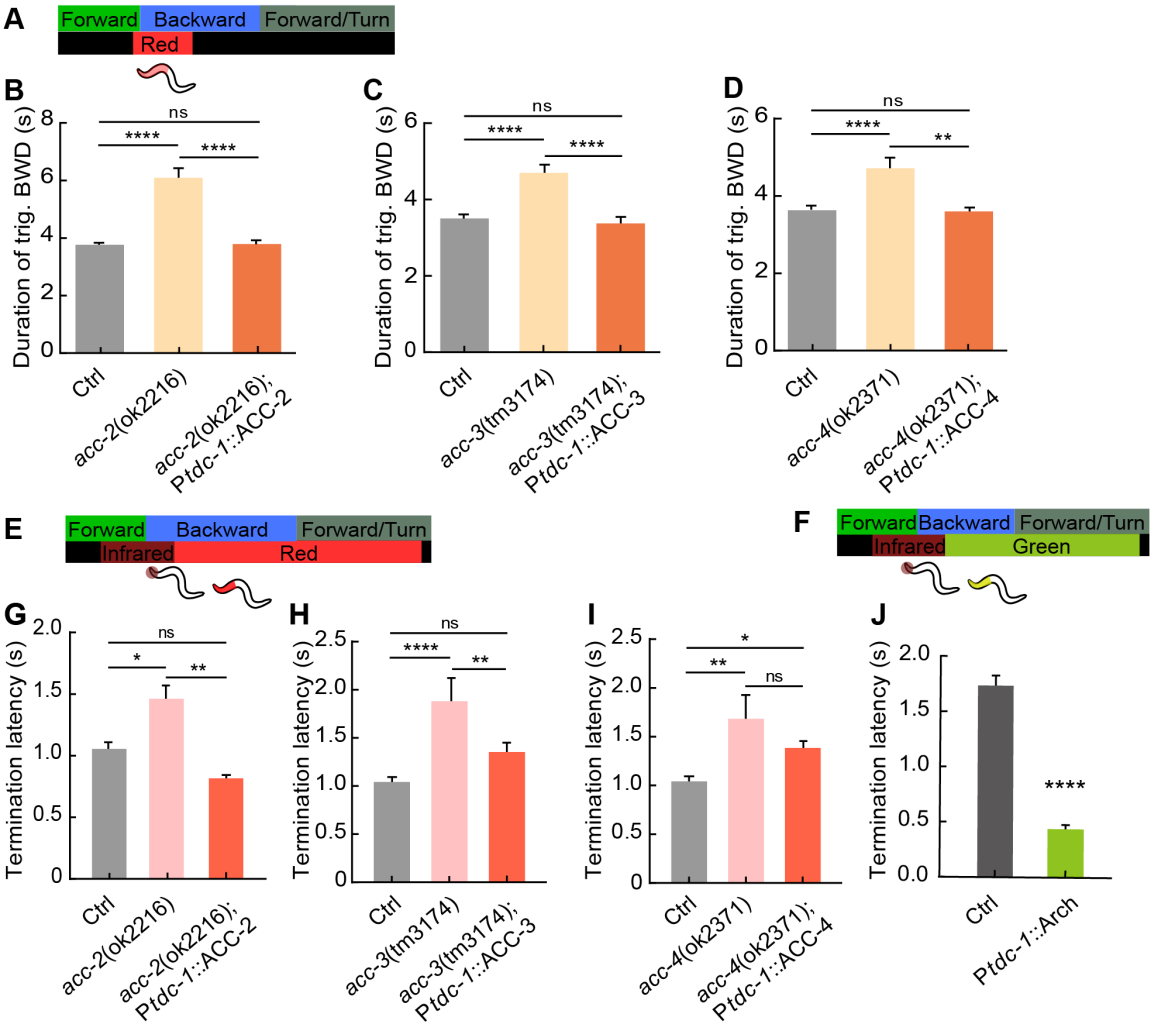

Figure S5. RIM communicates with SAA to terminate reversals via inhibitory acetylcholine synapses. **A.** Schematic experimental procedure for triggering escape responses, same as Fig. 4I. Optogenetic stimulation would activate AVM/ALM mechanosensory neurons. Related to **B**, **C**, and **D**. **B.** Duration of AVM/ALM-triggered reversal of control group, *acc-2* mutant and animals in which ACC-2 were specifically rescued in RIM. Ctrl: n = 414, 61 animals; *acc-2(ok2216)*: n = 88, 12 animals; *acc-2(ok2216)*;P*tdc-1::ACC-1*: n = 112, 19 animals. **C.** Duration of AVM/ALM-triggered reversal of control group, *acc-3* mutant and animals in which ACC-3 were specifically rescued in RIM. Ctrl: n = 414, 61 animals; *acc-3(tm3174)*: n = 88, 12 animals; *acc-3(tm3174)*;P*tdc-1::ACC-1*: n = 97, 11 animals. **D.** Duration of AVM/ALM-triggered reversal of control group, *acc-4* mutant and animals in which ACC-4 were specifically rescued in RIM. Ctrl: n = 414, 61 animals; *acc-4(ok2371)*: n = 123, 16 animals; *acc-4(ok2371)*;P*tdc-1::ACC-1*: n = 127, 21 animals. **E.** Schematic experimental procedure for activation of SAA/RIV/SMB during thermally induced escape responses, same as Fig. 5B. Related to **G**, **H**, and **I**. **G.** Termination latency in control, *acc-2* mutant, as well as animals in which ACC-2 was specifically restored in RIM. Ctrl: n = 229, 53 animals; *acc-2(ok2216)*: n = 103, 22 animals; *acc-2(ok2216)*;P*tdc-1::ACC-1*: n = 104, 19 animals. **H.** Termination latency in control, *acc-3* mutant, as well as animals in which ACC-3 was specifically restored in RIM. Ctrl: n = 229, 53 animals; *acc-3(tm3174)*: n = 126, 24 animals; *acc-3(tm3174)*;P*tdc-1::ACC-1*: n = 78, 14 animals. **I.** Termination latency in control, *acc-4* mutant, as well as animals in which ACC-4 was specifically restored in RIM. Ctrl: n = 229, 53 animals; *acc-4(ok2371)*: n = 141, 28 animals; *acc-4(ok2371)*;P*tdc-1::ACC-1*: n = 143, 26 animals. **F.** Schematic experimental procedure for inhibition of RIM during thermally induced escape responses. Reversal was triggered by an infrared laser (1480 nm, 50 mW/mm^2) focusing on the worm head for 1 s, followed by 7s green light optogenetic inhibition. Related to **J**. **J.** Termination latency between the onset of inhibiting RIM and the end of a reversal. Ctrl: n = 118, 19 animals; RIM::Arch: n = 85, 18 animals. All statistical tests: *P < 0.05, **P < 0.01, ****P < 0.0001, Mann–Whitney U test or Mann-Whitney U test with Bonferroni correction. Error bars represent SEM.

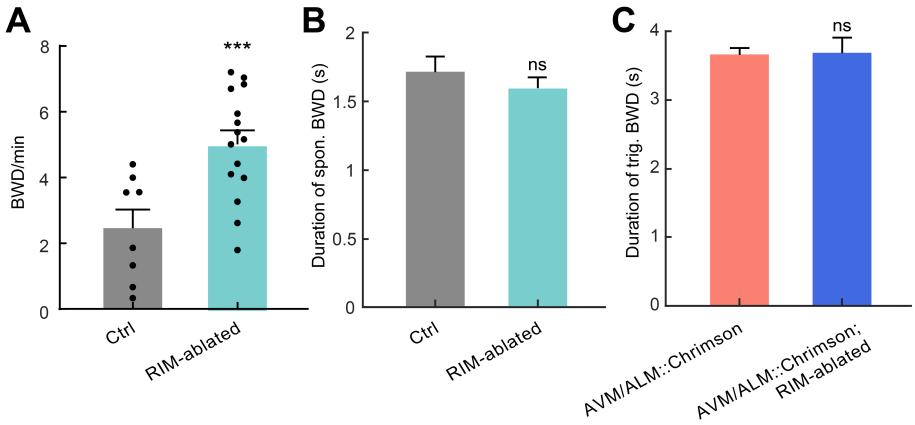

Figure S6. RIM-ablated animals make more frequent spontaneous reversals. **A.** Reversal frequency of control and RIM-ablated animals. Black dot represents an individual animal. Ctrl: n = 8 animals; RIM-ablated: n = 15 animals. **B.** Duration of spontaneous reversals in control and RIM-ablated animals are not significantly different. Ctrl: n = 112, 8 animals; RIM-ablated: n = 450, 15 animals. **C.** Duration of ALM/AVM triggered reversals in control and RIM-ablated animals are not significantly different. Ctrl: n = 414, 61 animals; RIM-ablated: n = 90, 17 animals. All statistical tests: Mann–Whitney U test, ***P < 0.001, error bars represent SEM.